

**Structural characterization and magnetic properties of $L1_0$ -
MnAl films grown on different underlayers by molecular beam
epitaxy**

Fumiya Takata¹, Toshiki Gushi¹, Akihito Anzai¹, Kaoru Toko¹, and Takashi Suemasu^{1,a)}

¹ *Institute of Applied Physics, Graduate School of Pure and Applied Sciences, University
of Tsukuba, Tsukuba, Ibaraki 305-8573, Japan*

^{a)} Electronic mail: suemasu@bk.tsukuba.ac.jp

ABSTRACT

We grow MnAl films on different underlayers by molecular beam epitaxy (MBE), and investigate their structural and magnetic properties. $L1_0$ -ordered MnAl films were successfully grown both on an MgO(001) single-crystalline substrate and on an $Mn_4N(001)$ buffer layer formed on MgO(001) and $SrTiO_3(001)$ substrates. For the MgO substrate, post rapid thermal annealing (RTA) drastically improved the crystalline quality and the degree of $L1_0$ -ordering, whereas no improvement in the crystallinity was achieved by altering the substrate temperature (T_S) during MBE growth. However, high-quality $L1_0$ -MnAl films were formed on the Mn_4N buffer layer by simply varying T_S . Structural analysis using X-ray diffraction showed MnAl on an MgO substrate had a cubic structure whereas MnAl on the Mn_4N buffer had a tetragonal structure. This difference in crystal structure affected the magnetic properties of the MnAl films. The uniaxial magnetic anisotropy constant (K_u) was drastically improved by inserting an Mn_4N buffer layer. We achieved a perpendicular magnetic anisotropy of $K_u = 5.0 \pm 0.7$ Merg/cm³ for MnAl/ Mn_4N film on MgO and 6.0 ± 0.2 Merg/cm³ on STO. These results suggest that Mn_4N has potential as an underlayer for $L1_0$ -MnAl.

Keywords:

A1 Crystal structure

A3 Molecular beam epitaxy

B1 MnAl

B1 Mn₄N

B1 MgO

B2 Magnetic materials

1. Introduction

Ferromagnetic thin films with perpendicular magnetic anisotropy (PMA) are of great interest in advanced spintronic devices such as spin-transfer-torque magnetic random access memory (STT-MRAM) with perpendicular magnetic tunneling junctions (*p*-MTJs). PMA materials possessing a large uniaxial magnetic anisotropy (K_u), low magnetic damping constant (α), and small saturation magnetization (M_S) are promising for realizing high thermal stability and low critical current density for STT switching of *p*-MTJs. Ordered binary alloys with an equiatomic ratio have been shown to be suitable as such materials. For instance, $L1_0$ - FePt, FePd, and CoPt exhibit a high magnetocrystalline anisotropy of the order of 10^7 erg/cm³ along the *c*-axis direction, and exhibits strong PMA [1-3]. Recently, Mn-based ordered alloys without noble or rare earth metals, such as $L1_0$ - and $D0_{22}$ - MnGa, have also attracted much attention as candidate materials [4,5]. Here, we focus on the $L1_0$ -MnAl ordered alloy. MnAl alloy have $L1_0$ -ordered structure in the compositional range of about 50–60 at. % Mn [6,7], and exhibits a large K_u ($> 1 \times 10^7$ erg/cm³), low α (~ 0.006), and relatively small M_S (< 600 emu/cm³), which are extremely desirable for an STT application [8-12]. In addition, a tunneling magnetoresistance (TMR) effect with a TMR ratio of 2% at room temperature (RT) was experimentally demonstrated in MTJs with an MnAl electrode [13]. A recent theoretical

calculation proposed a giant TMR effect in MnAl/MgO/MnAl stacks [14]. $L1_0$ -MnAl has lattice parameters of $a = 3.92 \text{ \AA}$ (in-plane) and $c = 3.57 \text{ \AA}$ (out-of-plane) [7]. The $L1_0$ structure can be reduced to the primitive structure regarded as a tetragonally distorted $B2$ type structure with lattice parameters of $\tilde{a} = 2.77 \text{ \AA}$ ($\tilde{a} = a/\sqrt{2}$) and $c = 3.57 \text{ \AA}$, and thus an axial ratio $c/\tilde{a} = 1.29$. In the present work, we used this primitive unit cell for structural analysis. Since the $L1_0$ -MnAl alloys are in a metastable phase (so-called τ -phase), the fabrication conditions, such as process temperature and the Mn/Al composition ratio, are crucial to obtain high-quality films. In this regard, it is also necessary to choose a suitable underlayer, such as one with a small in-plane lattice mismatch (Δf), good wettability, and less interfacial reaction, to realize high quality $L1_0$ -MnAl films. Moreover, although there have been many studies regarding the fabrication of $L1_0$ -MnAl films on several underlayers, for example, GaAs, Cr, TiN, and MgO [8-12], the growth of $L1_0$ -MnAl films on an underlayer with $\Delta f < 1\%$ has yet to be attempted.

In this study, we used MgO(001), MgAl₂O₄(MAO)(001), and SrTiO₃(STO)(001) single-crystalline substrates and an Mn₄N(001) buffer layer as underlayers, and investigated the dependence of the crystal growth and magnetic properties of an $L1_0$ -MnAl film on the underlayer species. The underlayers exhibited a different Δf with respect to $L1_0$ -MnAl, as shown in Table 1. Mn₄N has a cubic anti-

perovskite structure in which the Mn atoms occupy the corner and face-centered sites and an N atom is located at a body-center site. Mn_4N can be grown on MgO(001) and STO(001) substrates with a cube-on-cube epitaxial relationship and perfect lattice matching to $L1_0$ -MnAl when the MnAl lattice is rotated by 45° around the surface normal [15]. Mn_4N is ferrimagnetic with a very small M_S of 110 emu/cm^3 and has a perpendicular easy axis of magnetization ($K_u \sim 1.0 \times 10^6 \text{ erg/cm}^3$) that is independent of the underlayer substrate such as MgO(001), STO(001), and Si(001) [15-17]. While Mn_4N is ferromagnetic, it is considered that such properties do not seriously interfere with the magnetic behavior of the MnAl layer. Therefore, we propose that Mn_4N shows potential as an underlayer material for $L1_0$ -MnAl.

2. Experimental

MnAl films were grown on MgO(001), MAO(001), and STO(001) single-crystalline substrates and an $Mn_4N(001)$ buffer layer using a molecular beam epitaxy system equipped with Knudsen cells for the Mn and Al sources, and a radio-frequency (RF) N_2 plasma for the N source. The base pressure was less than 1×10^{-9} Torr. Prior to the growth, three kinds of substrates were first conventionally organically washed, and were then processed in different ways. The MgO and MAO substrates were thermally

cleaned at 600 and 900 °C for 30 min in an ultra-high vacuum, respectively. The STO substrates were dipped into a buffered HF solution (HF = 5 wt%, NH₄F = 35 wt%) to obtain an atomically flat surface before they were loaded into the MBE chamber [18]. A 5–10 nm-thick Mn₄N layer was fabricated on the MgO(001) and STO(001) substrates at a substrate temperature (T_S) of 450 °C as a buffer layer. The N₂ gas flow and RF input power were fixed to be 1.0 sccm (3.3×10^{-5} Torr) and 105 W, respectively [15]. A 15 nm-thick MnAl layer was grown at T_S of 100–400 °C. The Mn and Al deposition rates were controlled by the crucible temperatures so that the composition ratio of Mn to Al was close to 1 : 1. The total deposition rate was 0.8 nm/min. The films were *in-situ* covered with a 5 nm layer of SiO₂ or Ta at RT to prevent surface oxidation. After the deposition, rapid thermal annealing (RTA) was employed in a vacuum (lower than 1×10^{-3} Torr) at a post annealing temperature (T_A) of 150–400 °C for a few seconds to improve the chemical ordering of the MnAl layers. The crystalline qualities and structures were characterized by reflection high-energy electron diffraction (RHEED), ω - 2θ (out-of-plane) X-ray diffraction (XRD), and ϕ - 2θ (in-plane) XRD measurements with Cu- $K\alpha$ radiation. The magnetic properties were measured by a vibrating sample magnetometer at RT and a superconducting quantum interference device magnetometer at 300 K. The sample thickness was determined by X-ray reflectivity analysis.

3. Results and discussion

Figure 1 shows the RHEED patterns of the MnAl layer on (a) MgO(001), (b) MAO(001), and (c) STO(001) substrates grown at $T_S = 200$ °C, 150 °C, and 150 °C, respectively. A streaky RHEED pattern was obtained on the MgO substrates at $T_S = 200$ – 400 °C, showing that MnAl films were epitaxially grown on the MgO; however, other phases such as β -Mn became pronounced for samples formed at T_S much higher than 200 °C by XRD measurement. Therefore, we determined T_S to be 200 °C for MnAl films on MgO(001). In contrast, we could not achieve streaky RHEED patterns for samples on MAO and STO regardless of various T_S values in the range between RT– 300 °C. The RHEED streaks from MAO and STO substrates disappeared at the initial growth stage, probably owing to an interfacial reaction between MnAl and the substrates.

Figure 2 shows the T_A dependence of the out-of-plane XRD patterns of MnAl films on the MgO substrate grown at $T_S = 200$ °C. The diffraction peaks around $2\theta = 29.5^\circ$ and 61.3° correspond to the MnAl(001) and (002) planes, respectively. The (001)-oriented diffraction peaks indicate that the MnAl films were epitaxially grown on the MgO substrate with the c -axis normal to the sample surface. As described later in Fig. 3, the diffraction peaks of MnAl were labelled with "cubic" because they had a cubic

structure. The peak intensity of MnAl was drastically increased after the post RTA treatment even though it was difficult to improve the crystal quality of MnAl by varying T_S during MBE. Figure 3(a) shows the T_A dependence of the long-range order parameter (S) of $L1_0$ and the full width at half maximum (FWHM) for the MnAl(002) diffraction peak measured by the X-ray ω -scan rocking curve. The S was calculated from the intensity ratio of the $L1_0$ (001) superlattice diffraction to the (002) fundamental diffraction in the XRD patterns by using the following formula [19,20]:

$$S = \sqrt{\frac{I_{001}^{\text{obs}}/I_{002}^{\text{obs}}}{I_{001}^{\text{calc}}/I_{002}^{\text{calc}}}} \quad (1)$$

where I_{hkl}^{obs} and I_{hkl}^{calc} are the integrated intensities from the (hkl) plane obtained by experiment and calculation, respectively. The (001) superlattice diffraction peak appears when MnAl lattice forms the $L1_0$ -ordered structure. A value of $S = 1$ represents the perfectly ordered $L1_0$ phase. As shown in Fig. 3(a), S reached the largest value of 0.92 and the FWHM showed the smallest value of 0.11° at $T_A = 300^\circ\text{C}$. This indicates the formation of highly $L1_0$ ordered and oriented MnAl films on the MgO substrate by RTA. Figure 3(b) shows the in-plane XRD patterns of the MnAl films after annealing at $T_A = 300^\circ\text{C}$. The incident X-ray angle was fixed at $\omega = 0.4^\circ$ and the scattering vector (\mathbf{Q}) was set along MgO[200] and [220]. A sharp diffraction peak of MnAl(100) was observed when the \mathbf{Q} was set along the MgO[220] axis, while the peaks of MnAl(110) and (200)

were overlapped with those of the MgO substrate. These results show that the epitaxial relationship was $\text{MnAl}(001)[110] \parallel \text{MgO}(001)[100]$ as shown in Fig. 3(c). The lattice constants were calculated to be approximately $\tilde{a} = 3.00 \text{ \AA}$ ($a = 4.24 \text{ \AA}$) and $c = 3.02 \text{ \AA}$ by using the diffraction peak positions of the $\text{MnAl}(001)$, (002) , and (100) planes. The axial ratio of c/\tilde{a} was found to be almost 1.0, indicating that tetragonal MnAl transformed to a cubic structure owing to the very large Δf of -7% .

We next focus on the MnAl film on an Mn_4N buffer layer. We first discuss the MnAl films on $\text{Mn}_4\text{N}/\text{MgO}$. Figure 4(a) shows a typical RHEED pattern of the Mn_4N layer observed along the $\text{MgO}[100]$ azimuth. A clear streaky pattern together with superlattice streaks (shown by arrows in Fig. 4(a)), owing to the long-range order of N atoms at the body center position, was observed, meaning that a flat surface and high-quality Mn_4N epitaxial layer was obtained [21]. Figure 4(b) and 4(c) show the T_S dependence of RHEED patterns of the MnAl layer and out-of-plane XRD profiles of the $\text{MnAl}(15 \text{ nm})$ films on $\text{Mn}_4\text{N}(10 \text{ nm})/\text{MgO}$, respectively. Streaky RHEED patterns were observed at $T_S < 250 \text{ }^\circ\text{C}$, representing the epitaxial growth of MnAl films on the Mn_4N buffer. However, a ring RHEED pattern appeared at $T_S = 300 \text{ }^\circ\text{C}$. The XRD peaks at around $2\theta = 24.6^\circ$ and 50.31° originated from the $\text{MnAl}(001)$ and (002) planes, respectively. These peak positions were significantly different from those obtained on the

MgO substrate shown in Fig. 2. The peak intensity of MnAl became the largest at $T_S = 150$ °C, and they decreased with increasing or decreasing T_S . The diffraction peaks disappeared at 300 °C. This degradation of the crystalline quality was attributed to the atomic diffusions between the MnAl and Mn₄N layers at elevated T_S . Therefore, we determined the optimum T_S to be 150 °C for the growth of MnAl on Mn₄N underlayer. Figure 5(a) shows the T_S dependence of S and the FWHM values. The value of S was the largest of 0.91 at $T_S = 150$ °C and the FWHM reached a minimum of 1.28°. A highly oriented and $L1_0$ -ordered MnAl film was successfully obtained by simply varying T_S . On the other hand, however, we could not improve the $L1_0$ ordering by post RTA although we employed various T_A for samples grown at $T_S = 150$ °C. Figure 5(b) shows the in-plane XRD pattern of the MnAl film on Mn₄N/MgO grown at $T_S = 150$ °C. All the peaks from the MnAl layer were overlapped with those of the Mn₄N layer in the epitaxial relationship of MnAl(001)[110] || Mn₄N(001)[100].

Next, we discuss the MnAl films on Mn₄N/STO. We varied the T_S values in the range between 125 and 175 °C, and found out that $T_S = 150$ °C was optimum from the view point of S value. Figure 6 shows the out-of-plane XRD pattern of the MnAl(15 nm) film on Mn₄N(5 nm)/STO grown at $T_S = 150$ °C. The insets present the RHEED patterns of (a) Mn₄N and (b) MnAl layers of this sample, observed along the STO[100] azimuth.

The RHEED pattern of the Mn₄N layer was brighter than that from MgO (Fig. 4(a)) and Kikuchi lines appeared, revealing that a smooth Mn₄N layer of very high quality was epitaxied on the STO. This was associated with a small lattice mismatch between Mn₄N and STO ($\Delta f \sim 0.1\%$). The distinct XRD diffraction lines from the MnAl layer and their satellite peaks in Fig. 6 suggests the formation of a high crystallinity and flat MnAl layer. The FWHM of the MnAl(002) peak was a markedly small value of 0.08°. The better crystalline quality of the Mn₄N buffer layer promoted the excellent crystallinity of the MnAl layer. The calculated S value was 0.86, which is almost the same as that on Mn₄N/MgO. The lattice parameters of MnAl films on Mn₄N/MgO and on Mn₄N/STO were calculated to be $\tilde{a} = 2.77 \text{ \AA}$ ($a = 3.92 \text{ \AA}$), $c = 3.60 \text{ \AA}$, $c/\tilde{a} \sim 1.3$ and $\tilde{a} = 2.77 \text{ \AA}$ ($a = 3.92 \text{ \AA}$), $c = 3.61 \text{ \AA}$, $c/\tilde{a} \sim 1.30$, respectively. These lattice parameters are also almost the same as those of MnAl on Mn₄N/MgO and MnAl bulk.

Figure 7 shows the magnetization versus magnetic field (M - H) curves of MnAl films on (a) MgO ($T_S = 200 \text{ }^\circ\text{C}$, $T_A = 300 \text{ }^\circ\text{C}$), (b) Mn₄N(5 nm)/MgO ($T_S = 150 \text{ }^\circ\text{C}$), and (c) Mn₄N(5 nm)/STO ($T_S = 150 \text{ }^\circ\text{C}$). A magnetic field H was applied parallel (in-plane) and perpendicular (out-of-plane) to the film plane. On the MgO substrate (Fig. 7(a)), the magnetization curves were almost isotropic, and M_S was $360 \pm 20 \text{ emu/cm}^3$. The K_u was estimated to be approximately $0.9 \pm 0.1 \text{ Merg/cm}^3$ from the area enclosed between the in-

plane and out-of-plane magnetization curves and the demagnetization energy ($2\pi M_S^2$). The M_S and K_u were smaller than those of the bulk [7]. However, distinct PMA was obtained for MnAl on the Mn₄N buffer in Fig. 7(b) and 7(c), and a smooth and kink-free hysteresis loop indicated that MnAl and Mn₄N films were well exchange-coupled. The M_S of the ferromagnetic layer was 350 ± 30 emu/cm³ for MnAl/Mn₄N/MgO, and that of the MnAl layer with the contribution from Mn₄N ($M_S = 110$ emu/cm³) subtracted was estimated to be approximately 430 emu/cm³, which was close to the bulk value [7]. Moreover, a relatively large K_u of 5.0 ± 0.7 Merg/cm³ was achieved in the MnAl/Mn₄N film, which was comparable with those reported for MnAl films [11,12]. It can be stated that we successfully obtained a $L1_0$ -MnAl film with large PMA by inserting a Mn₄N buffer layer. Here, we consider a difference of the M_S and K_u in the MnAl film between on MgO and on Mn₄N underlayers. The differences were mainly attributed to the crystal structure of MnAl. According to a theoretical calculation, the magnetic moment of Mn and magnetocrystalline anisotropy of MnAl were greatly influenced by the axial ratio c/\tilde{a} and these values decreased through the transformation from a tetragonal to cubic structure [22]. Therefore, M_S and K_u decreased for the MnAl film on MgO. In comparison with Fig. 7(b), several notable magnetic properties appeared in Fig. 7(c), especially in magnetic anisotropy. The anisotropic magnetic field of MnAl/Mn₄N film on STO

exhibited an obviously larger value of about 50 kOe than that on MgO of 40 kOe. The estimated K_u also showed a larger value of 6.0 ± 0.2 Merg/cm³. Moreover, an out-of-plane remanence ratio (M_R/M_S) of 0.95 and a coercivity (H_C) of 7 kOe were obtained for this sample, while $M_R/M_S = 0.5$ and $H_C = 4$ kOe were obtained for MnAl/Mn₄N film on MgO. The substantial variance of the properties was mainly ascribed to the difference in crystallinity of the ferromagnetic layer. Higher crystal orientation gives rise to higher magnetic crystalline anisotropy in the MnAl layer. The larger H_C could also be interpreted by a high magnetic anisotropy. Furthermore, owing to the better crystal quality, the less defects in MnAl and Mn₄N could suppress the nucleation of magnetization reversal, resulting in the better squareness and smooth magnetization switching in those films [23,24]. These results show that better crystallinity of Mn₄N underlayer improved the magnetic properties of MnAl layer. On the other hand, however, the M_S of MnAl/Mn₄N/STO was as small as 270 ± 30 emu/cm³ (330 emu/cm³ for MnAl layer). Possible reasons for this small M_S are a slightly small S value of MnAl layer and a small deviation of Mn/Al composition ratio from the optimized one [25]. We believe that MnAl films using a Mn₄N underlayer can achieve higher PMA through more careful optimization of growth condition and Mn/Al composition. On the basis of our findings, it can be safely stated that inserting a Mn₄N underlayer is an effective means to improve

the S and K_u values of $L1_0$ -MnAl overlayers.

4. Conclusion

We investigated the influence of the underlayer on the crystal growth of $L1_0$ -MnAl, and characterized their structural and magnetic properties. $L1_0$ -MnAl films were successfully epitaxied on MgO(001) substrates and a Mn₄N(001) buffer layer, although they were unable to be directly grown on MAO(001) and STO(001) substrates epitaxially. On the MgO substrate, MnAl has a cubic crystal structure owing to the very large lattice mismatch, while the bulk-like tetragonal MnAl was formed on the lattice matching Mn₄N buffer. The difference of crystal structure significantly affected the magnetic properties of these films. A distinct PMA was realized for MnAl film on Mn₄N buffer layer. The better crystallinity of Mn₄N underlayer improved both crystalline quality and magnetic properties of the MnAl layer. A large PMA of $K_u = 6.0 \pm 0.2$ Merg/cm³ was obtained for MnAl/Mn₄N/STO. These results suggest that Mn₄N shows potential as an underlayer for $L1_0$ -MnAl.

Acknowledgements

Magnetization measurements were performed with the help of Professor H.

Yanagihara of the University of Tsukuba, and Associate Professor T. Koyano of Cryogenics Division of the University of Tsukuba.

Table 1 In-plane lattice constant a and \tilde{a} of underlayers and lattice mismatches (Δf) with respect to $L1_0$ -MnAl ($a = 3.92 \text{ \AA}$, $\tilde{a} = 2.77 \text{ \AA}$).

Underlayer	a [\AA]	\tilde{a} [\AA]	Δf [%]
MgO(001)	4.203	2.972	-6.73
MgAl ₂ O ₄ (001)	4.045	2.860	-3.09
SrTiO ₃ (001)	3.905	2.761	0.38
Mn ₄ N(001)/MgO(001)	3.90	2.758	0.51
Mn ₄ N(001)/SrTiO ₃ (001)	3.91	2.765	0.26

Figure captions

Figure 1 RHEED patterns after growth of a MnAl layer on (a)MgO, (b) MAO, and (c) STO(001) substrates. The incident electron beam was adjusted along the MgO[100] azimuth.

Figure 2 T_A dependence of the ω - 2θ XRD patterns of the MnAl film on a MgO substrate grown at $T_S = 200$ °C. The inset shows the RHEED pattern of the as-grown MnAl layer observed along the MgO[100] azimuth.

Figure 3 (a) T_A dependence of the order parameter (S) and FWHM for the MnAl(002) peak. (b) In-plane XRD profiles of the MnAl film on MgO annealed at $T_A = 300$ °C. The Q vector was set along MgO[200] (red) and [220] (green). (c) Schematic illustration of the epitaxial relationship of the MnAl film on a MgO(001) substrate.

Figure 4 (a) Typical RHEED patterns of the Mn₄N buffer layer on a MgO substrate. T_S dependence of (b) RHEED patterns of the MnAl layer and (c) ω - 2θ XRD patterns of MnAl/Mn₄N/MgO. The incident electron beam was directed along the MgO[100] azimuth.

Figure 5 (a) T_S dependence of the order parameter (S) and FWHM for the MnAl(002) peak. (b) In-plane XRD profiles of the MnAl film on Mn₄N/MgO grown at $T_S = 150$ °C. The Q vector was set along MgO[200] (red) and [220] (green).

Figure 6 ω - 2θ XRD patterns of the MnAl film on Mn₄N/STO grown at $T_S = 150$ °C. The inset figures are the RHEED patterns of the (a) Mn₄N and (b) MnAl layers observed along the STO[100] azimuth.

Figure 7 The M - H loops of magnetization for the (a) MnAl(15 nm)/MgO, (b) MnAl(15 nm)/Mn₄N(5 nm)/MgO, and (c) MnAl(15 nm)/Mn₄N(5 nm)/STO structures.

Reference

- [1] T. Klemmer, D. Hoydick, H. Okumura, B. Zhang, W. A. Soffa, *Scr. Metall. Mater.* 33 (1995) 1793.
- [2] V. Gehanno, A. Marty, B. Gilles, Y. Samson *Phys. Rev. B* 55 (1997) 12552.
- [3] M. R. Visokay, R. Sinclair, *Appl. Phys. Lett.* 66 (1995) 1692.
- [4] F. Wu, S. Mizukami, D. Watanabe, H. Naganuma, M. Oogane, Y. Ando, T. Miyazaki, *Appl. Phys. Lett.* 94 (2009) 122503.
- [5] S. Mizukami, T. Kubota, F. Wu, X. Zhang, T. Miyazaki, *Phys. Rev. B* 85 (2012) 014416.
- [6] H. Kono, *J. Phys. Soc. Jpn.* 13 (1958) 1444.
- [7] A. J. J. Koch, P. Hokkeling, M. G. Steeg, K. J. Vos, *J. Appl. Phys.* 31 (1960) 75S.
- [8] S. H. Nie, L. J. Zhu, J. Lu, D. Pan, H. L. Wang, X. Z. Yu, J. X. Xiao, J. H. Zhao, *Appl. Phys. Lett.* 102 (2013) 152405.
- [9] M. Hosoda, M. Oogane, M. Kubota, T. Kubota, H. Saruyama, S. Iihama, H. Naganuma, Y. Ando, *J. Appl. Phys.* 111 (2012) 07A324.
- [10] E. Y. Huang, M. H. Kryder, *IEEE Trans. Magn.* 51 (2015) 3401404.
- [11] L. Luo, N. Anuniwat, N. Dao, Y. Cui, S. Wolf, J. Lu, *J. Appl. Phys.* 119 (2016) 103902.
- [12] E. Y. Huang, M. H. Kryder, *J. Appl. Phys.* 117 (2015) 17E314.
- [13] H. Saruyama, M. Oogane, Y. Kurimoto, H. Naganuma, Y. Ando, *Jpn. J. Appl. Phys.* 52 (2013) 063003.
- [14] X. Zhang, L. L. Tao, J. Zhang, S. H. Liang, L. Jiang, X. F. Han, *Appl. Phys. Lett.* 110 (2017) 252403.
- [15] Y. Yasutomi, K. Ito, T. Sanai, K. Toko, T. Suemasu, *J. Appl. Phys.* 115 (2014) 17A935.
- [16] K. Kabara, M. Tsunoda, *J. Appl. Phys.* 117 (2015) 17B512.
- [17] K. Ching, W. Chang, T. Chin, *Appl. Sur. Sci.* 92 (1996) 471.
- [18] M. Kawasaki, K. Takahashi, T. Maeda, R. Tsuchiya, M. Shinohara, O. Ishiyama, T. Yonezawa, M. Yoshimoto, H. Koinuma, *Science* 266 (1994) 1540.
- [19] B. D. Cullity, *Elements of X-ray Diffraction*, Addison-Wesley, Reading, MA, 1956.
- [20] S. D. Granz, Mark H. Kryder, *J. Magn. Mater.* 324 (2012) 287.
- [21] K. Ito, S. Higashikozono, F. Takata, T. Gushi, K. Toko, T. Suemasu, *J. Cryst. Growth* 455 (2016) 66.
- [22] A. Sakuma, *J. Phys. Soc. Jpn.* 63 (1994) 1422.
- [23] J. P. Attane, Y. Samson, A. Marty, J. C. Toussaint, G. Dubois, A. Mougine, and J. P. Jamet, *Phys. Rev. Lett.* 93 (2004) 257203.
- [24] J. P. Attane, M. Tissier, A. Marty, and L. Vila, *Phys. Rev. B* 82 (2010) 024408.
- [25] M. Oogane, K. Watanabe, H. Saruyama, M. Hosoda, P. Shahnaz, Y. Kurimoto, M. Kubota, and Y. Ando, *Jpn. J. Appl. Phys.* 56 (2017) 0802A2.

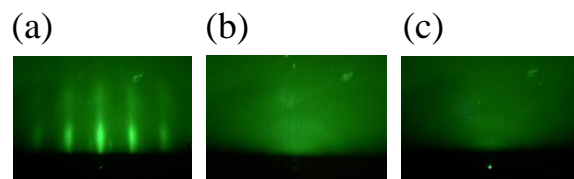


Fig. 1

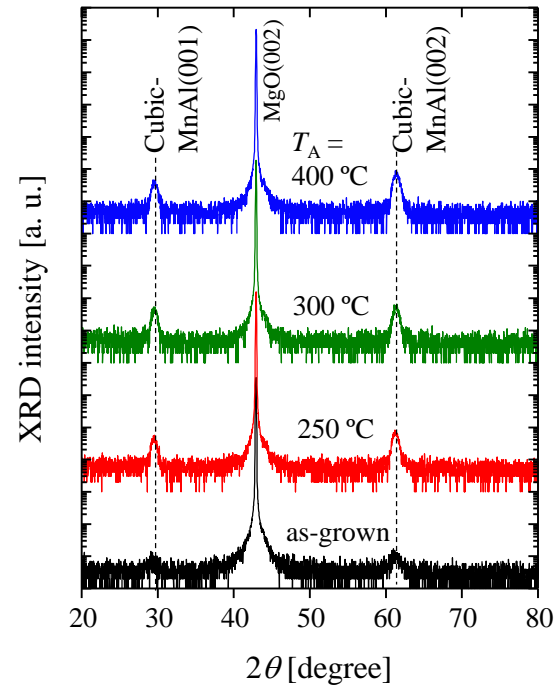


Fig. 2

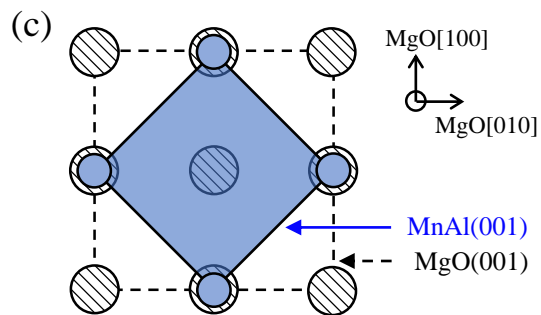
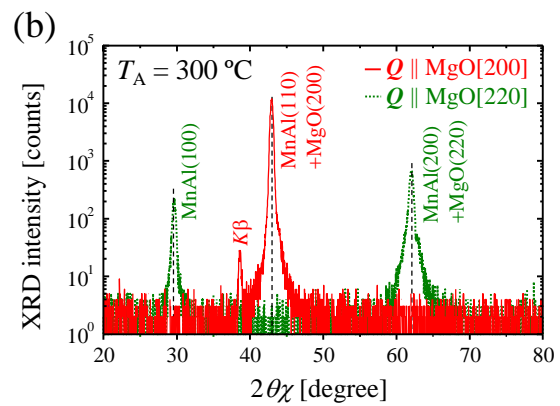
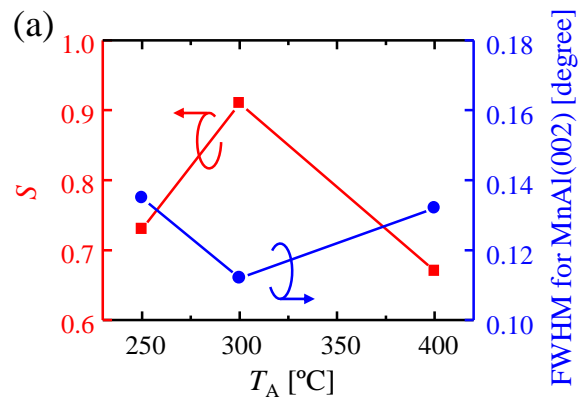


Fig. 3

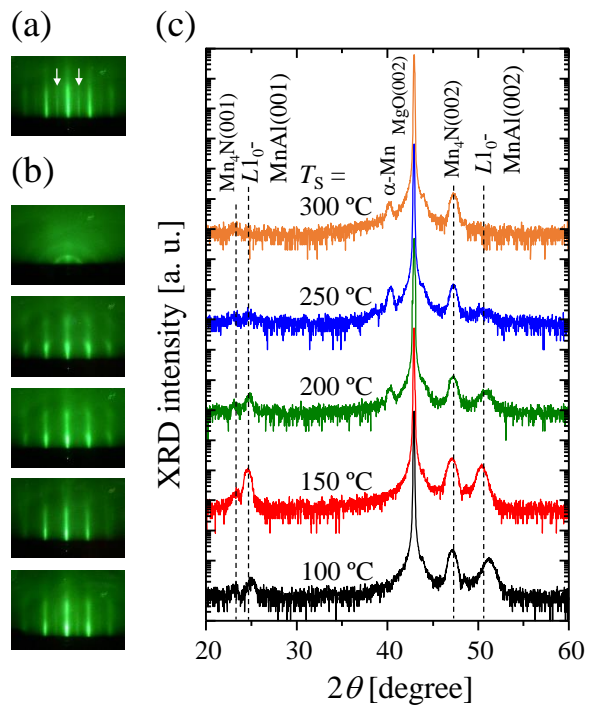


Fig. 4

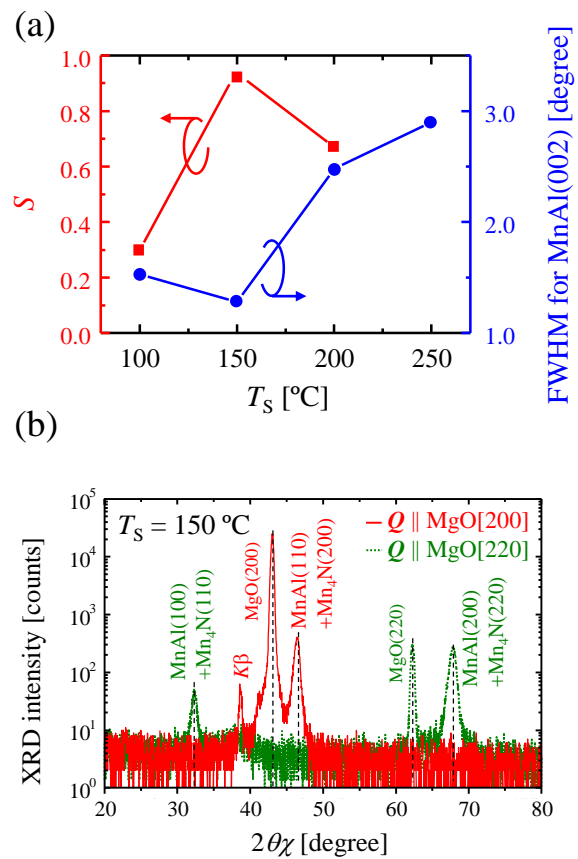


Fig. 5

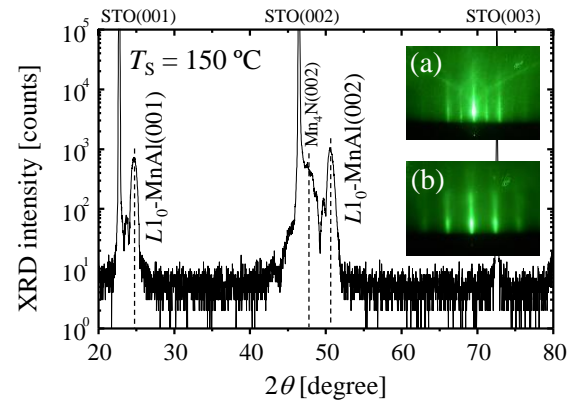


Fig. 6

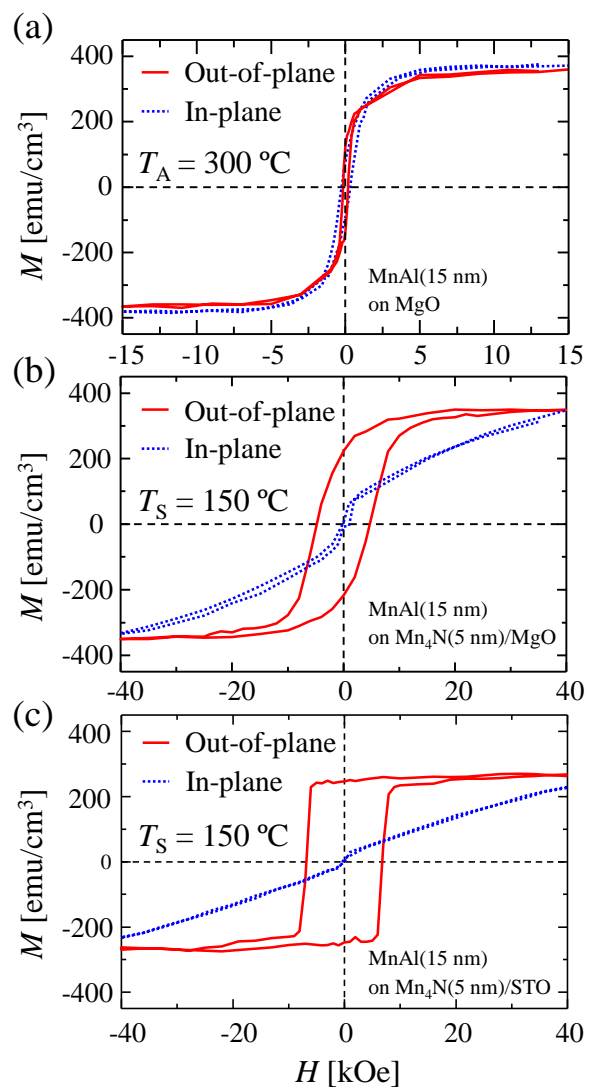


Fig. 7